Experimental NMRD Profiles for Some Low-Symmetry Ni(II) Complexes ($S = 1$) in Solution and Their Interpretation Using Slow-Motion Theory

Tomas Nilsson,[†,‡] Giacomo Parigi,[§] and Jozef Kowalewski*[,†]

Division of Physical Chemistry, Arrhenius Laboratory, Stockholm University, SE−106 91 Stockholm, Sweden, and CERM and Department of Agricultural Biotechnology, University of Florence, P.le delle Cascine 24, IT-50144, Florence, Italy

Received: October 31, 2001; In Final Form: February 12, 2002

Experimental NMRD profiles for four Ni(II) complexes ($S = 1$) in solution have been interpreted using slow-motion theory. Rhombicity in the zero-field splitting (ZFS) and noncoinciding static ZFS and dipole−dipole (DD) tensors are included in the model, which improves the physical picture in terms of the electronic structure and deformability of the complexes. In a previous study from our laboratory, $Ni(dpm)_2(aniline\text{-}d_5)_2^{2+}$ data were reported and analyzed using a model that assumed axially symmetric ZFS and coinciding static ZFS and DD tensors. These data are reinterpreted in the present article, which provides a nearly axially symmetric static ZFS. New experimental data on three aqueous solutions containing tetraaza complexes are also reported and interpreted. One of the systems, $Ni([15]aneN_4)(H_2O)_2^{2+}$, gives best-fit parameter values similar to those of $Ni(dpm)_2(aniline\text{-}d_5)_2^{2+}$. These two systems have the two solvent molecules coordinated in axial positions. The second complex, $Ni([12]aneN_4)(H_2O)_2^{2+}$, differs substantially in that the water molecules are coordinated in the cis configuration and that the best fit was obtained using a highly rhombic ZFS. The third complex, $Ni(tmc)(H_2O)^{2+}$, is five-coordinated, which results in a rather large rhombicity. In all cases, the best-fit parameters are clearly outside of the Redfield limit, which means that simpler theories are of limited use. We have also found that the latter two systems differ very much from the two former systems in terms of electron-spin dynamics. The main reason lies in the difference in the relative magnitudes of the static and the fluctuating transient parts of the ZFS, and this feature has a great impact on the rhombicity effect.

I. Introduction

Paramagnetic transition metal ions and complexes are characterized by the presence of an unpaired electron spin. The large magnetic moment associated with unpaired electrons interacts strongly with the nuclear magnetic moments through the hyperfine interaction. In a liquid solution, this interaction provides a highly efficient relaxation mechanism for nuclear spins and leads to the phenomenon of paramagnetic relaxation enhancement (PRE).[1] The PRE usually depends on the magnetic field used, and studies of proton spin−lattice relaxation as a function of magnetic field (nuclear magnetic relaxation dispersion, NMRD, studies) in solutions containing paramagnetic transition metal complexes have been an active area of research among chemists and biochemists for several decades.[2,3] In principle, such measurements can provide a wealth of information on structural and dynamical properties of transition metal complexes. In practice, the interpretation of the experimental NMRD profiles is often difficult because the theories available either have a limited validity range or are very complicated. In addition, even if measurements are carried out at a large number of different fields, the number of parameters may still be larger than the number of relevant features in the data.

The first step in the interpretation of NMRD profiles for paramagnetic solutions is rather simple: one has to understand the relation between the spin−lattice relaxation time for the ligand nuclei in the complex and the lifetime of the ligand in the complex. If the exchange lifetime is much shorter than the relaxation time, then the fast-exchange conditions hold,[4] and the PRE can be interpreted in terms of microscopic quantities characterizing the complex. The theoretical tools for further interpretation of NMRD profiles for paramagnetic solutions can be classified as belonging to a few general categories. First, there is the formalism known as modified Solomon−Bloembergen (MSB) equations, which is based on a simple description of dipolar and scalar relaxation processes in a two-spin system in combination with the Bloembergen−Morgan theory[5] of electron-spin relaxation.[2,3] The shortcomings of this model are well-known,[1] but it is nevertheless often used, for example, in discussions of contrast agents for magnetic resonance imaging.[6] The second group of methods correctly takes account of the fact that many complexes with $S = 1$ are characterized by sizable second-order spin−orbit coupling effects, accounted for in the spin-Hamiltonian formalism by the zero-field splitting (ZFS) term.[7] The general idea of the methods in this category can be traced to Lindner,[8] and different varieties have been proposed by Bertini and co-workers[1,2,9−11] and by Sharp.[12−16] The methods in this group assume that rotation and electron-spin relaxation are uncorrelated (this so-called decomposition approximation functions best in slowly reorienting systems) and make simplifying assumptions concerning the electron-spin relaxation. In a

* To whom correspondence should be addressed. E-mail: jk@physc.su.se. Tel: +44 8 162376. Fax: +44 8 152187.
† Stockholm University.
§ University of Florence.
‡ Present address: Department of Biophysical Chemistry, Lund University, SE-22000 Lund, Sweden.

10.1021/jp014010d CCC: $22.00
Published on Web 04/09/2002

recent article, a more theoretically satisfying description of the electron-spin relaxation has been included for $S = 1$.[17] Even this more sophisticated approach has rather severe limitations, as it requires the "strong narrowing conditions" or the Redfield limit[1] to be applicable. The third group of approaches can be called spin-trajectory methods, and an example has been proposed by Sharp.[18] This methodology circumvents the problem of the decomposition approximation. The most general approach, called slow-motion theory, has been developed in Swedish laboratories.[1,19] In its most recent varieties, the slow-motion theory can handle systems of arbitrary symmetry with $S = 1$[20] or higher.[21] No electron-spin relaxation times are explicitly defined, and the electron-spin dynamics is described in terms of complex rotational and distortional motions modulating the ZFS.

In this article, we report the applications of the recent version of the slow-motion theory to the interpretation of experimental data on some Ni(II) complexes. First of all, though, we illustrate a feature that is relevant to the analysis of experimental data. This feature concerns the electron-spin dynamics when the static and the fluctuating transient ZFS have comparable magnitudes and are outside of the Redfield limit. Consequently, slow-motion calculations are necessary for this purpose. Next, we use the experimental data sets for bis(2,2,6,6-tetramethyl-3,5-heptanedionato)Ni(II) (aniline-d_5)$_2$ (denoted in what follows as Ni(dpm)$_2$(aniline-d_5)$_2^{2+}$, complex I) published some years ago[22] and interpreted at that time using a more restricted version of the theory. In addition, we report new experimental results for aqueous solutions of three Ni(II) complexes with macrocyclic ligands: 1,4,8,12-tetraazacyclopentadecane ([15]aneN$_4$), 1,4,7,-10-tetraazacyclododecane ([12]aneN$_4$), and 1,4,8,11-tetramethyl-1,4,8,11-tetraazatetradecane, commonly called tetramethylcyclam (tmc). Ni([15]aneN$_4$)(H$_2$O)$_2^{2+}$ (complex II) displays the common trans configuration.[23] The [12]aneN$_4$ macrocycle, on the other hand, has a ring that is actually too small to accommodate the nickel ion in an optimal way.[23] As a result, the steric restrictions make it impossible for two water molecules in the Ni([12]aneN$_4$)(H$_2$O)$_2^{2+}$ complex (complex III) to access the metal ion on opposite sides of the macrocycle, and the two water ligands are therefore located cis to each other.[24] The tmc ligand has four very bulky methyl groups, which forces the Ni(II) complex to coordinate only one water molecule in an apical position.[25] Thus, Ni(tmc)(H$_2$O)$^{2+}$ (complex IV) is five-coordinated in a stable *R,S,R,S* configuration.[26] The four complexes considered (see Figure 1) thus form an interesting set of systems. Ni(dpm)$_2$(aniline-d_5)$_2^{2+}$ is dissolved in toluene-d_8/aniline-d_5, a mixed solvent that can be assumed to interact only weakly with the metal complex. The three aqueous tetraaza complexes can be expected to interact more strongly with the water solvent and to be more deformable. These three complexes contain macrocyclic ligands with different symmetries. The three complexes also have different symmetry, which should be reflected in different characteristics of the ZFS tensors. In all four systems, the chelating ligands are nonlabile, but the remaining ligands (aniline in Ni(dpm)$_2$(aniline-d_5)$_2^{2+}$ and water in the tetraaza systems) can be expected to exchange rapidly. Ni(dpm)$_2$(aniline-d_5)$_2^{2+}$ was earlier confirmed to be in the fast-exchange regime.

The outline of this article is thus as follows. In section II, we describe the experimental details for the tetraaza complexes. In section III, we review briefly the relevant theory and the computational method. In section IV, we show calculated NMRD profiles using slow-motion theory for some illustrative cases. Finally, the strategy employed for interpreting the experiments and the results of the least-squares fits of the new models to the experimental data is discussed in section V, and conclusions are drawn in section VI.

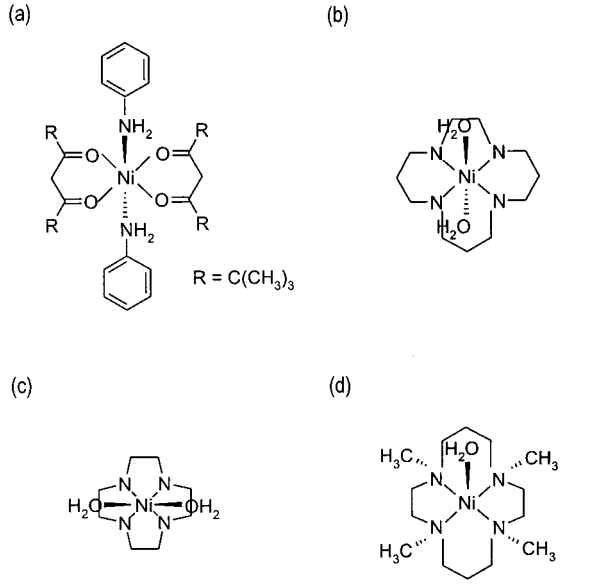

Figure 1. Low-symmetry Ni(II) complexes: (a) Ni(dpm)$_2$(aniline)$_2^{2+}$ (complex I), (b) Ni ([15]aneN$_4$)(H$_2$O)$_2^{2+}$ (complex II), (b) Ni([12]aneN$_4$)(H$_2$O)$_2^{2+}$ (complex III), and (c) Ni(tmc)(H$_2$O)$^{2+}$ (complex IV).

TABLE 1: Values of Concentrations, Coordination Numbers, and the Product $P_M q$ for the Different Complexes

complex	[solute], millimolal	[solvent], molal	q	$P_M q$
Ni(dpm)$_2$(aniline)$_2^{2+}$	1.74	1.16	2	0.300×10^{-2}
Ni([15]aneN$_4$)(H$_2$O)$_2^{2+}$	103.6	55.5	2	0.373×10^{-2}
Ni([12]aneN$_4$)(H$_2$O)$_2^{2+}$	109.7	55.5	2	0.395×10^{-2}
Ni(tmc)(H$_2$O)$^{2+}$	104.8	55.5	1	0.189×10^{-2}

II. Experimental Section

A. Preparation of Samples. The tetraaza complexes of nickel(II) and zinc(II) have been prepared as perchlorate salts. The zinc analogues have been used for carbon-13 spin−lattice relaxation time measurements, which provide an estimate of the rotational correlation time. Nickel(II) perchlorate hexahydrate, zinc(II) perchlorate hexahydrate, and the ligands [12]aneN$_4$, [15]aneN$_4$, and tmc were purchased from Sigma-Aldrich and used without further purification. Ni(tmc)(ClO$_4$)$_2$ was synthesized according to the method described by Barefield and Wagner,[25] and the same method was used for Ni([12]aneN$_4$)(ClO$_4$)$_2$ and Ni([15]aneN$_4$)(ClO$_4$)$_2$. An excess of ligands was removed by dissolving the products in deionized water, cooling in a refrigerator overnight, and filtering. The filtrate was then evaporated to dryness, washed, and dried again as described in ref 25. The corresponding zinc complexes were prepared in exactly the same way. Deionized water was used for the NMR samples, and all other solvents were of analytical grade and were used without further purification. The purity was checked by NMR and UV−vis spectroscopy, and the spectra were in agreement with values reported in the literature.[25−31]

Caution: Perchlorate salts of metal complexes can be explosive and must be handled with care.

B. Relaxometry Measurements. The concentration of the solutions was about 100 mM (see Table 1). Two different field-cycling relaxometers were used, covering different regions of low magnetic fields. The water proton relaxation-rate measurements in the paramagnetic solutions at very low fields (up to

about 0.4 T, which corresponds to a 15-MHz proton resonance frequency) were carried out with a Stelar field-cycling relaxometer and 10 mm tubes for the samples. The polarizing field was 0.23 T, and the echo was detected at 0.15 T, corresponding to 10 and 6.5 MHz, respectively. For measurements between 0.23 and 0.4 T (10−15 MHz), no polarizing field was needed.

A Koenig-Brown field-cycling relaxometer was used to make measurements at fields between 0.4 and 1.2 T (15−50 MHz). The same samples used for the Stelar relaxometry measurements were also used here after transferring the samples to another type of 10-mm tube. The polarizing field was 1.04 T (45 MHz), and the measuring field was 0.104 T (4.5 MHz). No polarizing field was required above 0.52 T (22.5 MHz).

C. Proton Spin−Lattice Relaxation Measurements. D_2O was added (for field-frequency lock) to the solutions used at low field (D_2O/H_2O, 1/5), and the solutions were then transferred to standard 5-mm NMR tubes. The different concentrations in the low- and high-field measurements were taken into account, assuming a linear variation of the PRE with concentration. The relaxation-rate measurements at higher fields were carried out with Bruker MSL 90, MSL 200, DMX 500, and DMX 800 spectrometers operating at 2.1, 4.7, 11.8, and 18.8 T, respectively. At the highest fields, the probe head was detuned slightly to minimize the problems due to radiation damping of the extremely strong water signal. In addition, a gradient was used to further minimize the problem from radiation damping.[32] An inversion−recovery sequence with at least 10 different delays was used, and the spin−lattice relaxation rate was evaluated using three-parameter fitting routines included in the standard spectrometer software.

D. Carbon-13 Spin−Lattice Relaxation Measurements. The zinc complexes were dissolved in D_2O and transferred to standard 10-mm NMR tubes. The samples were then degassed by several freeze−pump−thaw cycles and sealed under vacuum. The carbon-13 experiments were performed on a Varian Inova 400 NMR spectrometer operating at 9.4 T using the fast inversion−recovery technique and decoupling the protons by means of the Waltz-16 modulation. The carbon-13 90° pulse was about 16 μs, the spectral widths were 6500 and 200 Hz, and the number of data points was 12 600 and 400 for complexes II and III, respectively. The ^{13}C spectrum of Zn([12]aneN$_4$)-$(H_2O)_2^{2+}$ consisted of a single line, indicating the chemical equivalence of all of the carbons. The Zn([15]aneN$_4$)-$(H_2O)_2^{2+}$ sample, on the other hand, displayed at least 18 resonances. This result is in agreement with the observation of Hung et al.[30] that the corresponding Co(III) complex occurs in solution in the form of two isomers that are characterized by a large number of nonequivalent carbon sites. The rotational correlation time for the Zn([15]aneN$_4$)$(H_2O)_2^{2+}$ complex was estimated from the average T_1 value. Because of the similar sizes of complexes II and IV (the molecular weight of IV is, however, somewhat larger than that of II), we estimated the rotational correlation time for complex IV from that of Zn([15]-aneN$_4$)$(H_2O)_2^{2+}$. We validate this assumption in section V.

All experiments described above were run at 298 K, with the temperature controlled by standard variable-temperature accessories delivered by the instrument manufacturers. The relaxation rates were converted into PRE by subtracting the diamagnetic rate (0.4 s^{-1}).

III. Slow-Motion Theory

The slow-motion theory has been described in several reviews and articles[19−22,33,34] and is summarized only briefly here. In particular, a recent article[20] contains the relevant equations.

A. Nuclear-Spin Relaxation in Paramagnetic Systems. It is assumed that the nuclear-spin relaxation is caused by weak coupling to the lattice, which makes the Wangsness−Bloch−Redfield (WBR) theory, or simply the Redfield theory,[35−39] appropriate to use for the nuclear spin system. The electron spin system, on the other hand, is treated together with classical degrees of freedom (reorientation and distortion) in the slow-motion theory as a composite lattice. The PRE of ligand protons in a solution of a paramagnetic transition-metal complex is caused by modulation of the hyperfine interaction between the nuclear spins and the unpaired electron spins. This hyperfine interaction consists of the through-space dipole−dipole (DD) interaction and the Fermi contact (or scalar) interaction. Only the DD interaction is considered in this article because the contribution from the Fermi contact interaction is generally assumed to be rather small for proton-spin−lattice relaxation. The DD interaction is described by the following Hamiltonian

$$H_{IL}^{DD} = \sum_n (-1)^n I_n^1 T_{-n}^1 \qquad (1)$$

where I_n^1 are the components of a standard rank-one irreducible spherical tensor operator[40] for the nuclear spin and T_n^1 are the components of the lattice tensor operator, which is written as a scalar contraction of a standard rank-one irreducible spherical tensor operator for the electron spin with components S_q^1 and the Wigner rotation matrix of rank two with elements $D_{0,n-q}^2[\Omega_{ML}(t)]$. The equation that defines the lattice tensor operator can be found in ref 20. The Wigner rotation matrix elements describe the transformation from the molecule-fixed frame (M frame) to the laboratory frame (L frame) through the set of Euler angles Ω_{ML}. The angles Ω_{ML} describe the orientation of the dipole−dipole tensor with respect to the external magnetic field, whose direction is defined as the z axis of the laboratory frame. T_n^1 also contain the dipole−dipole coupling constant and thus the distance R between the nuclear spin and the paramagnetic center.

By using Redfield theory and the Liouville space superoperator formalism,[41,42] we obtain the expression for the nuclear-spin−lattice relaxation rate of ligand nuclei bound to the paramagnetic site as the real part of the complex spectral density taken at the nuclear spin Larmor frequency:

$$T_{1,I}^{-1} = 2Re\{K_{1,1}^{DD}(-\omega_I)\} \qquad (2)$$

The spectral density in eq 2 is given by the Fourier−Laplace transform

$$K_{1,1}^{DD}(-\omega_I) = \int_0^\infty \mathrm{Tr}_L\{T_1^{1\dagger} e^{-i\mathcal{L}_L\tau} T_1^1 \rho_L^{eq}\} e^{-i\omega_I\tau}\, d\tau \qquad (3)$$

where the autocorrelation function for the lattice, which is the expression within the trace, contains the lattice tensor operators, T_1^1, the lattice density operator,[43] ρ_L^{eq}, which is assumed to be in thermal equilibrium at all times, and the lattice Liouville superoperator, $\mathcal{L}_L$ (lattice Liouvillian), which determines the time evolution of the system. Next, we turn to a description of the lattice dynamics.

B. Lattice Dynamics. In the present model, the lattice Liouvillian is defined by the following terms

$$\mathcal{L}_L = \mathcal{L}_S + \mathcal{L}_R + \mathcal{L}_D + \mathcal{L}_{ZFS}^S + \mathcal{L}_{ZFS}^T \qquad (4)$$

where $\mathcal{L}_S$ is the Liouville superoperator generated by the electron-spin Zeeman Hamiltonian, $H_S = \omega_S S_z$ (the sign of the electron-spin Larmor frequency ω_S is, by convention, taken to

be the same as that of the magnetogyric ratio γ_S). Furthermore, $\mathcal{K}_R$ and $\mathcal{K}_D$ are Markov operators describing the molecular reorientation (R) and distortion (D) of the complex as isotropic rotational and pseudorotational diffusion, respectively. These operators include the characteristic reorientational correlation time τ_R and the distortional correlation time τ_D, both corresponding to rank-two spherical harmonics. The last two terms in eq 4 describe the coupling between the electron spin system and the classical degrees of freedom (the thermal reservoir). Both Liouvillians are generated by the corresponding Hamiltonians. Clearly, there is only one ZFS Hamiltonian or Liouvillian at any instant. The two terms in eq 4 reflect the assumptions that the modulation of the ZFS occurs on two time scales. $\mathcal{K}^S_{ZFS}$ describes the static ZFS interaction, which represents an average over the fast processes (vibrations, collisions) and is subject to reorientational modulation. The static ZFS has a strong influence on the energy-level fine structure, especially at low magnetic fields.

$\mathcal{K}^T_{ZFS}$ describes the transient ZFS interaction. The transient ZFS has its origin in the distortions of the paramagnetic complex because of collisions with surrounding solvent molecules. Its dynamics is modeled as a pseudorotational diffusion. As seen from the molecular frame, the static and transient ZFS represent the mean and the spread, respectively, of the total ZFS.[20] Under slow rotational conditions, the pseudorotational modulation of the transient ZFS becomes the dominating mechanism for the electron-spin relaxation.

The Hamiltonians of the static and transient ZFS are given explicitly in ref 20. Briefly, both Hamiltonians contain components of a standard rank-two irreducible spherical tensor operator for the electron spin S^2_{-n} and components of the static and transient ZFS tensor, respectively. In addition, each of the Hamiltonians contains two sets of Wigner rotational matrix elements. One of the sets is common to both operators: $D^2_{m,n}[\Omega_{ML}(t)]$ describes the transformation from the M to the L frame (the same as in T^1_n). The second set in the static ZFS Hamiltonian, $D^2_{l,m}[\Omega_{P_SM}]$ describes the transformation from the principal axis system of the static ZFS tensor (P_S frame) to the M frame. In the transient ZFS Hamiltonian, these are replaced by $D^2_{k,m}[\Omega_{P_TM}(t)]$, describing the transformation from the principal axis system of the transient ZFS tensor (P_T frame) to the M frame. The difference between the two sets of Euler angles is that $\Omega_{P_SM} = (\alpha_{P_S}, \beta_{P_S}, 0)$ are treated as time-independent parameters having a simple relationship with the spherical polar angles θ and ϕ so that $\alpha_{P_S} = \phi$ and $\beta_{P_S} = \theta$. These angles define the orientation of the dipole−dipole tensor with respect to the principal axis system of the static ZFS tensor.

It is customary to define the symmetric and traceless ZFS tensor in terms of the axial (D) and rhombic (E) parameters.[7] The relationships between the irreducible spherical components of the two ZFS tensors and their axial and rhombic parameters can be found in a previous article.[20] The relationship between the magnitude of the static ZFS Δ_S and the tensor components D_S and E_S is $\Delta^2_S = {}^2/_3 D^2_S + 2E^2_S$. By analogy to the static ZFS, the magnitude and components of the transient ZFS tensor are related by $\Delta^2_T = {}^2/_3 D^2_T + 2E^2_T$.

C. Computational Method. To evaluate the spectral density at the nuclear-spin Larmor frequency (cf. eq 3), we need its matrix representation, which is obtained by expanding the lattice tensor operators T^1_n in an orthonormal basis set defined in the Liouville space. The Liouville basis set and the projection vectors have been given previously in Appendix A of ref 20. Once we have set up the supermatrix $\mathbf{M} = i(\mathbf{L}_L + \omega_I \mathbf{1})$ (see Appendix B in ref 20), the computational problem amounts to finding its inverse, which yields the expression for the nuclear-spin−lattice relaxation rate:

$$T_{1,I}^{-1} = \frac{4}{3}(C^{DD})^2 S(S+1) Re\{c_1^* \mathbf{M}^{-1} c_1\} \qquad (5)$$

Because the projection vectors c_1 contain only three nonzero elements for the DD interaction (see Appendix B in ref 20), a 3×3 fragment of the inverse supermatrix $\mathbf{M}^{-1}$ is sufficient. The supermatrix $\mathbf{M}$ is sparse, and its size, which in principle is infinitely large because of the classical degrees of freedom, depends on the convergence properties in the inversion routine. The inversion of $\mathbf{M}$ is performed numerically by means of the Lanczos algorithm.[44] The size of the supermatrix is increased step-by-step (by increasing the quantum numbers L and A; cf. ref 20) until convergence of the desired accuracy is accomplished.

The algorithm for the nonlinear least-squares fitting is based on the FORTRAN subroutine STEPIT.[45] The algorithm GENLSS[46] (FORTRAN code) was used for estimating error limits of the fitted parameters. These subroutines have been modified to work together with the slow-motion computer program on IBM SP2 parallel computers. Most of the computations have been performed on parallel computers (IBM SP2). However, in some cases, we also used an ordinary PC (two 180 MHz Pentium processors) with extended RAM memory (512 MB).

IV. Results of Slow-Motion Calculations

In this section, we present some NMRD profiles where we illustrate the effects of rhombicity in the transient ZFS. The aim is to focus on a feature in the electron-spin dynamics for which the rhombicity in the transient ZFS is of central importance, but we also discuss the effects of having a static ZFS tensor of rhombic symmetry. In these cases, some of the parameters are held fixed with values appropriate for the experimental analysis in the following section. The distance between the nuclear and electron spins R is set to 3 Å, the reorientational correlation time τ_R takes the value 60 ps, and the distortional correlation time τ_D is set to 10 ps. Furthermore, we assume an isotropic g tensor with an effective value of 2.25.

A. Physical Picture of the Rhombicity Effects. Before starting to discuss the cases of low-symmetry complexes, we should say something about the physical interpretation of the transient ZFS tensor of rhombic symmetry, starting with complexes of high symmetry (e.g., O_h). From a combined ab initio quantum chemical calculation and molecular dynamics simulation study, Odelius et al.[47] investigated the time fluctuations in the ZFS tensor for Ni(II) ions ($S = 1$) in aqueous solution. They found the distribution of ZFS eigenvalues to display three peaks, indicating that the triplet manifold was split into three levels by a fully rhombic transient ZFS. The main contribution to the rhombicity in the fluctuating ZFS was due to damped vibrations (of E_g and T_{2g} symmetries) in the complex, which suggests that the transient ZFS tensor induced by damped vibrational motions will probably be of rhombic symmetry for all kinds of complexes.

In the slow-motion theory presented in this article, the physical interpretation of having a transient ZFS tensor of rhombic symmetry can be viewed as an approximate representation of damped vibrational motions in the lattice. The axial symmetry in the transient ZFS means that only an isotropic distortional motion of the ligand framework is present, which is modeled as an isotropic pseudorotational diffusion. On the other hand, if the transient ZFS has rhombic symmetry, it reflects

the anisotropy in the electron-spin dynamics induced by damped vibrational motions (i.e., an effective description of a combined motion caused by isotropic distortional diffusion and anisotropic damped vibrations).

For clarity, the physical origins of the rhombicity effect in the static and transient ZFS should also be distinguished at this stage. Complexes with symmetry lower than tetragonal (D_4) or trigonal (D_3) on average have a static ZFS tensor with rhombic symmetry,[7,15,48] which can affect the PRE very dramatically, as we discussed in a previous article.[20] The rhombicity effect and its consequences for PRE were originally pointed out by Fukui et al.[49] for $S = 1$ and $^3/_2$ and were independently reported by Sharp[13] for $S = 1$. Sharp and co-workers gave the physical interpretation of the phenomenon[13−15] for $S = 1$, $^3/_2$, and 2. The transient ZFS of rhombic symmetry in complexes of arbitrary average symmetry can occur because of a combined effect of collisions with solvent molecules (e.g, water) and damped vibrational motions.[47] The consequences for PRE are rather different for the static and transient ZFS effects, and they also depend on the motional regime. In the slow-rotation situation, the static ZFS gives primarily an energy-level effect or it affects the electron-spin dynamics described by nonstochastic processes (i.e., precessional motions) whereas the transient ZFS influences the electron-spin dynamics described by stochastic processes (i.e., electron-spin relaxation). In rapidly reorienting complexes, on the other hand, both static and transient ZFS effects (including the ZFS rhombicity) can influence electron-spin relaxation. Yet another different situation arises in the slow-motion regime ($\tau_D\omega_{\Delta_T} \gtrsim 1$) if the magnitude of the transient ZFS is larger than or comparable to that of the static ZFS, which is discussed in detail below.

B. Effects of Rhombicity in the Transient ZFS. We now discuss two cases where the effects of rhombicity in the transient ZFS tensor are investigated (with and without static ZFS rhombicity present). In the first case, the magnitude of the static ZFS tensor Δ_S is 5 cm^{-1}, and that of the transient ZFS tensor Δ_T is 1 cm^{-1}, corresponding to a highly asymmetric and deformable complex. In the second case, Δ_S is 1 cm^{-1} and Δ_T is 2 cm^{-1}, corresponding to a slightly asymmetric and highly deformable complex. The main difference between these two cases lies in the relative magnitudes of Δ_S and Δ_T. In the first case, the static ZFS dominates the transient ZFS, whereas in the second case, the magnitude of the transient ZFS is larger than that of the static ZFS. The rhombicity effects in these two situations are rather different. The calculated NMRD profiles were obtained in such a way as to keep the magnitude of the transient ZFS tensor constant while varying the rhombic parameter E_T between 0 and $^1/_3D_T$ (the maximum possible value). The magnitude of the static ZFS tensor was held constant in the same way when E_S was varied between 0 and $^1/_3D_S$. The combined rhombicity effect is shown under the condition of the principal axis systems of the static ZFS and the dipole−dipole tensors coinciding; thus, the polar angles θ and ϕ are set to zero.

The NMRD profiles in Figure 2 show the effect of rhombicity in the transient and static ZFS. In Figure 2a, we show these effects for the case of Δ_S dominating over Δ_T. At low magnetic fields, the electron-spin principal axis is fixed in the molecule, and if the rhombic term E_S is zero (solid lines), we can speak of a molecule-fixed quantization axis of the electron spin. However, if rhombicity is introduced, then the permanent magnetic dipole moment disappears because the rhombic term causes the electron-spin principal axis to fluctuate in time. This rhombicity effect, which quenches the coupling between the nuclear and electron spins and causes the PRE to be reduced almost to zero at low magnetic fields, has been discussed earlier by us[20] and by several others.[13−15,49] The influence of increasing the rhombicity in the transient ZFS is minor, which is evident from Figure 2a, especially if rhombicity in the static ZFS is present (the two dotted curves coincide). Clearly, if Δ_S dominates over Δ_T, the electron-spin dynamics is more sensitive to rhombicity effects in the static ZFS than it is in the transient ZFS, which is reflected in the PRE changes in Figure 2a.

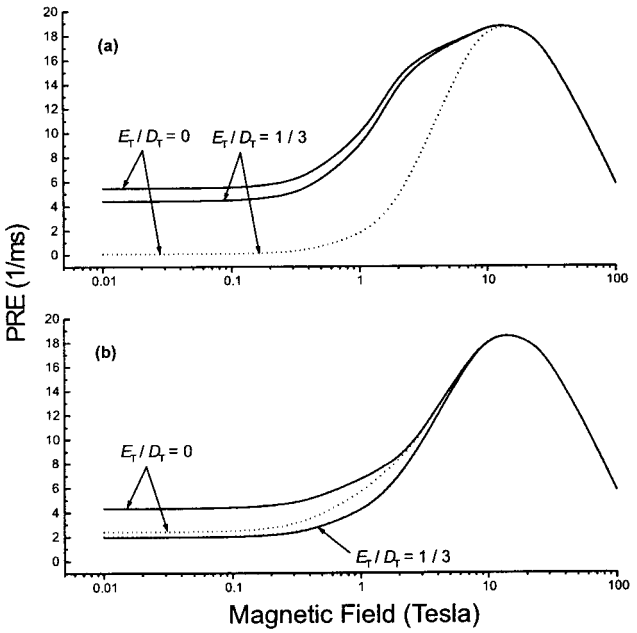

Figure 2. Calculated NMRD profiles showing rhombicity effects for (a) the case when Δ_S (5 cm^{-1}) dominates Δ_T (1 cm^{-1}) and (b) the case when Δ_T (2 cm^{-1}) is larger than Δ_S (1 cm^{-1}). The solid lines correspond to $E_S/D_T = 0$, and the dotted lines refer to $E_S/D_T = 1/3$. Other parameter values are given in the text.

In Figure 2b, we show the rhombicity effects for a case where Δ_T is larger than Δ_S. In this situation, we cannot speak of a molecule-fixed quantization axis at low magnetic fields, irrespective of the presence or absence of rhombicity in the static ZFS. The reason is that if the transient part momentarily dominates over the static part under slow-motion conditions ($\tau_D\omega_{\Delta T} \gtrsim 1$) then the energy-level structure can at each instant be considered to be determined by the transient rather than the static part. The fluctuating transient ZFS tensor is, of course, not fixed in the molecule; consequently, neither is the energy-level structure. In this picture, the rhombicity of the transient ZFS takes over the role of the rhombicity of the static ZFS in other situations as the cause of the suppression of the unique quantization axis of the electron spin in the molecular frame, leading to the rapid precessional motion of the electron spin. That motion has the effect of reducing the coupling between the nuclear and electron spins and the PRE. We can thus see that allowing the same type of symmetry breaking in both the static and the transient ZFS leads to an intricate interplay of different effects. The feature regarding rhombicity effects in this case is that the E_T term influences the PRE more than does the E_S term. This behavior, in particular, the negligible effect of changing the value of E_S in the presence of rhombicity in the transient ZFS (the two profiles with the smallest low-field plateaus that almost coincide) is seen in Figure 2b. The sensitivity of the electron-spin dynamics to rhombicity in the ZFS is opposite to that of the first case (Figure 2a). Thus, rhombicity in the transient ZFS has a greater influence on the

PRE than it does in the first case. This influence would be even more pronounced if Δ_T clearly dominated Δ_S (not shown). We will see both types of cases, corresponding to Figures 2a and b, in the analysis of the experimental data of Ni complexes in the following section.

V. Experimental Results and Analysis

Under fast-exchange conditions,[50,51] the measured ligand proton relaxation rates and the relaxation rate in the paramagnetic complex are related to each other by the expression

$$T_1^{-1}(\text{para}) - T_1^{-1}(\text{dia}) = T_{1,\text{P}}^{-1} = \frac{P_M q}{\tau_M + T_{1,\text{I}}} \approx P_M q T_{1,\text{I}}^{-1} \qquad (6)$$

where T_1^{-1}(para) is the relaxation rate of the ligand proton in a paramagnetic solution, T_1^{-1}(dia) is the corresponding rate in a diamagnetic solution, and $T_{1,\text{P}}^{-1}$ is the PRE. P_M is the mole fraction of the transition-metal complex, q is the coordination number (i.e., the number of exchangeble ligand molecules in the complex), and τ_M is the lifetime of the exchangeble ligands. Fast-exchange conditions (i.e., $\tau_M \ll T_{1,\text{I}}$) were previously proved to prevail in the Ni(dpm)$_2$(aniline-d_5)$_2^{2+}$ complex.[22] In the tetraaza complexes, we observed a reduction of the PRE upon increasing the temperature at high magnetic fields, indicating that eq 6 is also valid in these cases, at least in the high-field region. The concentrations of the paramagnetic solutes and the solvents used in the relaxometry experiments, together with the values of the product $P_M q$ for the different complexes, are given in Table 1.

In the next section, we outline the strategy that we have employed to extract the information about the electron spin system. Thereafter, we present and discuss the results for each complex separately.

A. Strategy for Interpreting Experimental NMRD Profiles. A theoretical model such as the slow-motion theory, which is capable of interpreting NMRD profiles for low-symmetry Ni(II) complexes, of course includes several parameters. It is a formidable task to determine all of them, and one way of dealing with this problem is to focus on just a few. In the first place, we neglect the outer-sphere relaxation (the influence of the paramagnetic ion on the relaxation of ligand protons outside of its first coordination sphere). We have chosen to focus on the electron spin system and, in particular, the ZFS parameters (D_S, E_S, and D_T) together with the distortional dynamics described by τ_D and the distance R between the nuclear and electron spins (under the point-dipole approximation,[52] the electron spin is assumed to reside at the site of the metal ion). This set of parameters was chosen at the expense of some of the other parameters being determined less accurately. There is a limited number of other sources that can be used to determine some of the parameters used in the slow-motion theory. Knowledge about the electron spin system is not directly obtainable through EPR measurements on systems for which the electron-spin relaxation is in the slow-motion regime because the ESR line shape is simply too broad.[53] Thus, for the Ni(II) complexes that we have studied, which are slow-motion cases, there is scant information in the literature in terms of the parameters included in the slow-motion theory. The assumptions that we invoke to deal with the other parameters will now be discussed.

The electronic g factor is assumed to be isotropic, with the value 2.25 (the same value that was used previously for the Ni(II) hexa-aqua complex[54] and for the Ni(dpm)$_2$-(aniline-d_5)$_2^{2+}$ system[22]). The reorientational correlation time τ_R has been determined for the corresponding Zn(II) complex by carbon-13 spin−lattice relaxation measurements (see ref 22 for Zn(dpm)$_2$(aniline-d_5)$_2^{2+}$ and the Experimental Section for the zinc tetraaza complexes). The Zn(II) complexes are chemically very similar to the Ni(II) analogues in terms of ionic radius and charge, and thus we assume that the reorientational motion also behaves similarly. The estimated values of τ_R for the different Ni(II) complexes at specified temperatures are given in Table 2.

TABLE 2: Estimated Values of τ_R at a Certain Temperature and of θ for the Different Complexes

complex	τ_R (ps)	θ (deg)
Ni(dpm)$_2$(aniline)$_2^{2+}$	170 (at −11 °C)	15
Ni(dpm)$_2$(aniline)$_2^{2+}$	90 (at 10 °C)	15
Ni(dpm)$_2$(aniline)$_2^{2+}$	50 (at 32 °C)	15
Ni([15]aneN$_4$)(H$_2$O)$_2^{2+}$	66 (at 25 °C)	13
Ni([12]aneN$_4$)(H$_2$O)$_2^{2+}$	45 (at 25 °C)	43
Ni(tmc)(H$_2$O)$^{2+}$	70 (at 25 °C)	13

Crystallographic data for Ni([12]aneN$_4$)(H$_2$O)$_2^{2+}$ are available,[24] and using this information we have estimated the polar angle θ for this complex. The values of θ for the other three complexes were estimated by simple geometrical considerations and are given in Table 2. Thus, we assume that the static ZFS principal axis is oriented along the principal symmetry axis of the complex (i.e., in the direction of the overall tetragonal distortion). Under this assumption, we consider it unlikely that the estimated values of θ for complexes I, II, and IV differ by more than 1 or 2 degrees. For complex III, on the other hand, the deviation may be up to 15° because this complex has a cis configuration. Thus, the symmetry axis, which we assume to coincide with the ZFS principal axis, falls between the two Ni−O bonds, whereas in the other complexes, the symmetry axis is in the direction of the Ni−O bond. A more correct picture of the orientation of the DD tensor relative to that of the static ZFS tensor in complex III may be obtained by taking into account a distribution of θ values. This approach, however, results in excessively cumbersome calculations and inconveniently large computer time requirements. By using the value of θ given in Table 2, we describe the average behavior in the orientation of the DD and static ZFS tensors. However, we found that this parameter is rather insensitive to the fitting, and thus the actual value is of minor importance.

The azimuthal angle ϕ and the rhombic transient ZFS parameter E_T are assumed to be of minor significance on the basis of a previous report concerning calculated NMRD profiles,[55] and thus it is reasonable to set their values equal to zero. We validate this assumption for each complex in the sections that follow. In fact, the assumption of an axially symmetric transient ZFS seems untenable for at least one of the complexes, which is discussed below.

Even parameters that we determine by the fitting procedure may be affected by the assumptions in the strategy. The determined value of the distance R should, for example, be regarded with caution because it may be influenced by several factors. First, we have neglected the contribution from outer-sphere relaxation, which may be up to 30% of the total PRE,[56] so by neglecting this contribution, the value of R determined by fitting may be 5% too small. Second, the assumed value of the g factor (2.25) may be incorrect: a 10% change in the g factor would change R by about 3%. In addition, the g tensor may be anisotropic, which may further change the value of R somewhat. However, because the primary aim of the present investigation is to determine ZFS parameters and distortional dynamics, we may regard the distance R in combination with the g factor, which are both included in the DD coupling

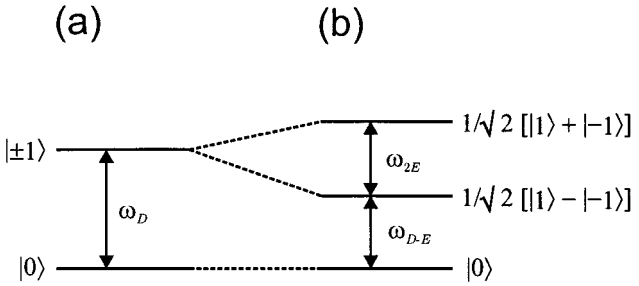

Figure 3. Energy-level diagram for $S = 1$ in the low-field limit for the cases of (a) axial static ZFS and (b) rhombic static ZFS.

constant, simply as a combined scaling factor. In this way, we absorb any ambiguities due to the aforementioned assumptions into the parameter R.

Consequently, the remaining parameters that we can adjust in the nonlinear least-squares fittings are the static ZFS parameters D_S and E_S, the transient ZFS parameter D_T, the distortional correlation time τ_D, and the distance R. By performing a series of four-parameter trial fittings, varying the four adjustable parameters from the parameter space (D_S, E_S, D_T, τ_D, R), we found that the value of D_S remained relatively constant. In the fittings where Δ_S dominates Δ_T, we found that D_S did not change much at all, which is in agreement with the findings of Sharp and co-workers.[16,57] For the cases where Δ_S and Δ_T are of similar magnitude, the value of D_S changed slightly. From these findings, we decided to keep D_S fixed in the final fittings, with the values obtained from the trials. Because our aim is primarily to investigate the rhombicity effect, we feel fairly safe in making this assumption.

The rationale of the insensitivity of the D_S parameter in the fittings may be clarified by showing the so-called power-density plots.[12,58] A power-density plot is a graphical interpretation of the nuclear-spin dipolar power density (i.e., the PRE efficiency), which is obtained by plotting the dipolar spectral density $k(\omega_i - \omega)$ as a function of ω, where ω_i correspond to the characteristic electron-spin transition frequencies in the low-field limit (i.e., 0 and ω_D for an axial static ZFS and ω_{2E} and $\omega_{D\pm E}$ for the rhombic case). The energy-level diagram for $S = 1$ in the low-field regime showing the transition-frequencies is depicted in Figure 3. Unfortunately, we cannot use $K^{DD}_{1,1}(-\omega_I)$ in eq 3 to obtain all the necessary components $k(\omega_i)$ because it can yield only the sum of $k(\omega_{D+E})$ and $k(\omega_{D-E})$. The reason for this is that the electron-spin energy part is not separated from the remaining lattice in the slow-motion theory. However, we may use the low-field expressions given in a previous article.[59] We show in Figure 4 the power-density plots of the spectral densities $k(\omega_i)$. The plots are similar to the results of Sharp and co-workers.[12,58] The spectral densities are centered at their corresponding frequencies (e.g., $k(\omega_D)$ at $\omega = \omega_D$). The PRE efficiency is proportional to the power density at $\omega = \omega_I$, which may be regarded as zero frequency on the electronic frequency scale. It is evident from the power-density plot in Figure 4 that the dominant mechanism is provided by $k(0)$ in the axial case and by $k(\omega_{2E})$ in the rhombic case. The power peak centered at ω_{2E} contributes a significant zero-frequency power density, which makes the E_S parameter important in the fitting procedure, whereas the power peaks at $\omega_{D\pm E}$ have negligible zero-frequency power densities, and thus the D_S parameter becomes less important in the fitting procedure. It should be mentioned that the widths of the power peaks are dependent on τ_D, which strongly influences how much zero-frequency power density the spectral densities contribute. We checked with the slow-motion theory to confirm that the line widths of $k(\omega_{2E})$ and the

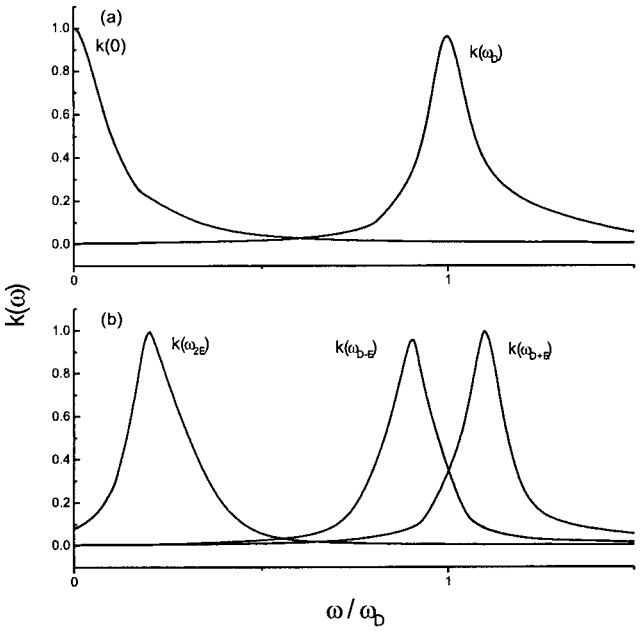

Figure 4. Power-density plot for $S = 1$ in the low-field limit for the cases of (a) axial ($E_S/D_S = 0$) and (b) rhombic ($E_S/D_S = 1/10$) static ZFS. The other parameter values are $\Delta_S = 5$ cm^{-1}, $\Delta_T = 1$ cm^{-1}, $\tau_D = 4$ ps, and $\tau_R = 1$ μs.

sums of $k(\omega_{D+E})$ and $k(\omega_{D-E})$ did not change appreciably by increasing τ_D from 4 to 10 ps.

The number of different features in the NMRD profiles is limited, in practice, to not more than three (the low-field plateau, the frequency at which the PRE starts to increase, and the steepness of the increase). Thus, we decided to carry out final three-parameter fittings (R, τ_D, E_S) for a series of fixed values of D_T rather than to perform four-parameter fittings. However, we did some four-parameter final fittings by admitting rhombicity in the transient ZFS (D_T was then adjustable for certain E_T/D_T ratios). Moreover, we reduced the number of points (10−14) in the fittings to save computational time, retaining only enough data to characterize the shape of the NMRD profiles with some confidence. In principle, only points in the flat low-field region were left out, and thus all the high-field data were used. We should also mention that the algorithm STEPIT[45] that we have used for the fitting procedure does not provide error limits for the fitted parameters. To estimate these limits, we used another algorithm, GENLSS.[46] The strategy here was to take the final parameter values from the STEPIT-based fitting as starting values in the GENLSS-based fitting and to let GENLSS run for one iteration. The reason we did not use GENLSS for the whole fitting procedure was that we had serious problems with convergence. We will now turn to the presentation and discussion of the experimental results.

B. Reinterpretation of Ni(dpm)$_2$(aniline-d_5)$_2^{2+}$ Data. We begin with the reinterpretation of Ni(dpm)$_2$(aniline-d_5)$_2^{2+}$, of which we have some prior knowledge from a previous investigation at our laboratory.[22] A set of constrained three-parameter nonlinear least-squares fittings for different D_T values was performed under the assumption of a fixed D_S value of 5.0 cm^{-1}. The experimental data were obtained at three different temperatures (−11, 10, and 32 °C) in the quoted investigation, and we start by discussing the analysis for the case of the lowest temperature.

The best-fit values for this complex at −11 °C are reported in Table 3. Moreover, we show the experimental NMRD profile in Figure 5 together with the fitted curve using the best-fit values

TABLE 3: Constrained Three-Parameter (R, τ_D, E_S) Nonlinear Least Squares Fitting at Different Values of D_T for Ni(dpm)$_2$(aniline)$_2^{2+}$ at −11 °C a Using Fixed Value of D_S (5.0 cm^{-1})

	D_T				
	1.5	1.6	1.7	1.8	2.0
R (Å)	3.52 ± 0.03	3.52 ± 0.02	3.52 ± 0.04	3.52 ± 0.04	3.52 ± 0.03
τ_D (ps)	8.1 ± 1.1	9.4 ± 2.2	11 ± 5	13 ± 8	17 ± 6
E_S (cm^{-1})	0.081 ± 0.006	0.012 ± 0.003	0.005 ± 0.005	0.003 ± 0.001	0.005 ± 0.001
σ	0.1053	0.1008	0.0942	0.1062	0.1391

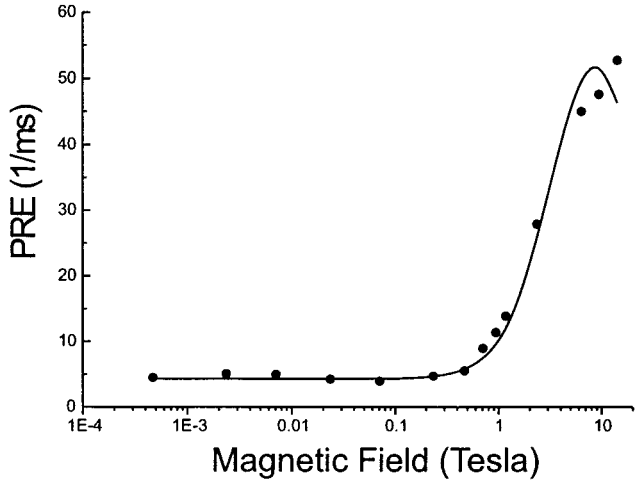

Figure 5. Experimental (symbols) and fitted (line) NMRD profiles for Ni(dpm)$_2$(aniline)$_2^{2+}$ at −11 °C. All available experimental points are used in the fittings and are shown as filled symbols. The fitted curve has been calculated on the basis of the best-fit data in Table 3 for D_T = 1.7 cm^{-1}.

reported in Table 3 for D_T = 1.7 cm^{-1}. These values are rather similar to those obtained in ref 22. These investigators estimated the magnitude of the static ZFS to be about 5 cm^{-1}, corresponding to D_S = 6.1 cm^{-1}, whereas we assumed a value of 5.0 cm^{-1} for D_S. The overall symmetry of the complex is tetragonal, and thus it presumably has a rather large axial component of the static ZFS. We found the rhombic component E_S to have a very small value of about 0.005 cm^{-1}, indicating that the assumption of an axial static ZFS tensor made in the previous study is justified by our present analysis. Clearly, the obtained values of R are the same (3.52 Å) in the set of fittings given in Table 3. This distance is somewhat longer than that obtained in ref 22, which is 3.48 Å. This difference is mainly due to the inclusion of the symmetry-breaking properties θ and E_S (less important) in the latest version of the slow-motion theory. Also interesting is that the value of τ_D obtained here (about 11 ps) is only slightly lower than the result in ref 22 (about 13 ps). In addition, the previous study found a slightly larger value of D_T (1.8 cm^{-1}) compared to ours (1.7 cm^{-1}).

The best-fit values for this complex at 10 °C are reported in Table 4. We show the experimental NMRD profile in Figure 6 together with the fitted curve using the best-fit values reported in Table 4 for D_T = 1.8 cm^{-1}. These values are also similar to those in the previous study. The distance is somewhat longer (3.38 Å) and the distortional correlation time slightly shorter (11 ps) in the present analysis than those found in the previous study (R = 3.34 Å and τ_D = 14 ps). In addition, the value of D_T is found to be only slightly lower (1.8 cm^{-1}) here than that found previously (1.9 cm^{-1}). The value of E_S has increased by a factor of about four to 0.02 cm^{-1} compared to the value at the lower temperature, but it is still rather small. This result is most likely an effect of a reduced sensitivity of this parameter in the fitting procedure when its value is so small.

The best-fit values at 32 °C are reported in Table 5. We show the experimental NMRD profile in Figure 7 together with the fitted curve using the best-fit values reported in Table 5 for D_T = 2.4 cm^{-1}. These values, as for those at the other temperatures, are similar to those in the previous study. The values of R and τ_D are found to be 3.13 Å and 5.6 ps, respectively, in the present study, which is slightly higher for R and lower for τ_D than for the previous results (R = 3.12 Å and τ_D = 7.1 ps). For the transient ZFS parameter D_T, we obtain the same value as in the previous analysis (2.4 cm^{-1}). The value of E_S has increased by an order of magnitude to 0.05 cm^{-1} compared to the lowest-temperature value, but this is, again, probably due to the aforementioned insensitivity.

The temperature dependence of τ_D seems to be somewhat better in the present study than in the previous investigation. The value of τ_D can be expected to decrease with increasing temperature; this decrease was not seen in the previous study, whereas here we obtain 11 ps at both −11 and 10 °C and a reduction to 5.6 ps at 32 °C. Furthermore, the values obtained in the present study are all slightly lower than those of ref 22, and a lower value of τ_D seems to agree better with the distortional correlation times reported in earlier work on paramagnetic complexes.[57,60] Although changes in the correlation time with temperature are expected, the reasons for the variation of R with the temperature are not completely clear. One possible explanation might be that the fast-exchange condition, which was established to be valid at a field strength of 2.35 T,[22] may perhaps be violated at low temperature and low magnetic field. A consequence of such a violation would be an underestimation of the nuclear-spin relaxation contribution to the PRE (i.e., $T_{1,I}$), which would in turn produce a scaling factor that was too small for the whole curve or an R value that was too large.

We have fitted the NMRD profiles using L = 6 (the principal quantum number of the reorientational basis set) to achieve convergence in the final fittings, whereas in the trial fittings, we also used L = 4. Thus, increasing the value of L means that we increase the size of the supermatrix and hence come closer to full convergence. The convergence properties and, in particular, the size of the reorientational basis are sensitive to the magnitude of the static ZFS because reorientation is the motion that modulates this interaction. We found in the trial fittings that the value of D_S diminishes if L is increased from 4 to 6 but that the other parameters do not change appreciably for the case of θ = 15°. We also tried two values of θ in the trial fittings to study its importance. The difference between assuming that θ = 15° and 0° is that the values of D_S and τ_D change somewhat but are within the error limit for the latter parameter. We checked the effects of varying the parameters ϕ and E_T using the best-fit values in Tables 3−5 for D_T = 1.7, 1.8, and 2.4 cm^{-1}. We found that varying ϕ gives negligible changes in the PRE and that introducing rhombicity in the transient ZFS changes the PRE very little.

C. Interpretation of Ni([15]aneN$_4$)(H$_2$O)$_2^{2+}$ Data. The best-fit values of the restricted fittings for Ni([15]aneN$_4$)(H$_2$O)$_2^{2+}$

TABLE 4: Constrained Three-Parameter (R, τ_D, E_S) Nonlinear Least Squares Fitting at Different Values of D_T for Ni(dpm)$_2$(aniline)$_2^{2+}$ at 10 °C a Using Fixed Value of D_S (5.0 cm^{-1})

	D_T				
	1.5	1.6	1.7	1.8	1.9
R (Å)	3.38 ± 0.03	3.38 ± 0.02	3.38 ± 0.03	3.38 ± 0.02	3.38 ± 0.02
τ_D (ps)	7.4 ± 2.5	8.8 ± 3.9	10 ± 5	11 ± 5	13 ± 6
E_S (cm^{-1})	0.2 ± 0.1	0.12 ± 0.06	0.07 ± 0.04	0.02 ± 0.02	0.006 ± 0.006
σ	0.0916	0.0881	0.0868	0.0858	0.0906

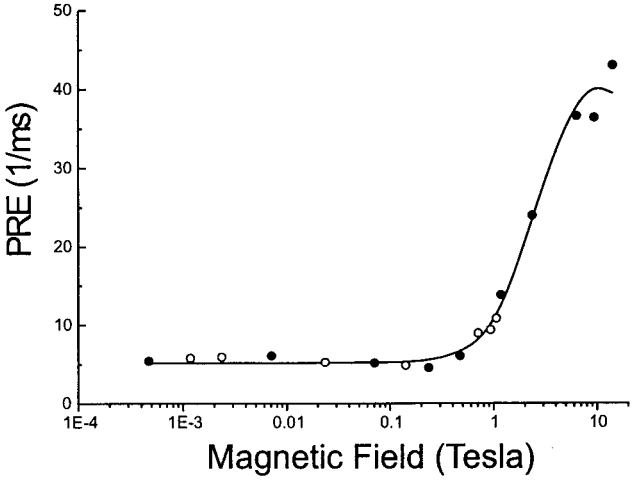

Figure 6. Experimental (symbols) and fitted (line) NMRD profiles for Ni(dpm)$_2$(aniline)$_2^{2+}$ at 10 °C. Experimental points used in the fittings are shown as filled symbols. The fitted curve has been calculated on the basis of the best-fit data in Table 4 for $D_T = 1.8$ cm^{-1}.

using different values of D_T are collected in Table 6. In these fittings, we assumed the same value (5.0 cm^{-1}) for D_S as for Ni(dpm)$_2$(aniline-d_5)$_2^{2+}$. In Figure 8, we show the experimental NMRD profile of this complex together with the fitted curve corresponding to the best-fit values reported in Table 6 for the case of $D_T = 2.3$ cm^{-1}. The best-fit parameter values are rather similar to those obtained for Ni(dpm)$_2$(aniline-d_5)$_2^{2+}$. The rhombicity is, for example, very similar in the tetraaza complex at 25° C with an E_S value of 0.05 cm^{-1} to that of Ni(dpm)$_2$(aniline-d_5)$_2^{2+}$ where E_S is 0.02 cm^{-1} at 10 °C and 0.05 cm^{-1} at 32 °C. Thus, both these complexes seem to have negligibly small rhombicity, which is not unreasonable because of the overall tetragonal symmetry.

The tetraaza complex has a D_T value of 2.3 cm^{-1}, which is between the values for complex I at the two highest temperatures (1.8 cm^{-1} at 10 °C and 2.4 cm^{-1} at 32 °C). In addition, the obtained value of τ_D (10 ps) is similar to that obtained for Ni(dpm)$_2$(aniline-d_5)$_2^{2+}$ at 10 °C (11 ps). This similarity implies that these two complexes have approximately the same flexibility or deformability, which may be explained as follows. The tetraaza complex has a macrocyclic ligand, which may be expected to make it more rigid. The other complex, on the other hand, has two open chelate ligands, which may be more flexible. However, Ni(dpm)$_2$(aniline-d_5)$_2^{2+}$ is dissolved in a mixed organic solvent (toluene-d_8/aniline-d_5) whereas the tetraaza complex is in aqueous solution, and one can expect the water molecules to interact more strongly than do organic molecules with the complex. This behavior indicates that the tetraaza complex should be the more flexible of the two. The net effect may be that these two contributions cancel so that the overall flexibility is rather similar in the two complexes, as we have found.

Also, for this complex, we fitted the profile using two values of θ (0° and 13°) and two values of L (4 and 6) in the trials. The only noticeable difference in the parameter values between these four fittings is that of D_S in the case of $\theta = 0°$ and $L = 6$. Thus, the fitting of the NMRD profile of this complex does not seem to be very sensitive to either a change in L (i.e., the calculated PRE has converged) or a change in θ. We also checked the effects of varying the parameters ϕ and E_T for this complex using the best-fit data given in Table 6 for $D_T = 2.3$ cm^{-1}, and the changes in the PRE are very similar to those for Ni(dpm)$_2$(aniline-d_5)$_2^{2+}$.

D. Interpretation of Ni([12]aneN$_4$)(H$_2$O)$_2^{2+}$ Data. The Ni([12]aneN$_4$)(H$_2$O)$_2^{2+}$ complex differs from the other two systems (complexes I and II) in two ways. Structurally, the fact that the two oxygen ligands (water molecules) are cis to each other creates a ligand field of lower symmetry (C_{2v}). However, the overall symmetry of the complex may be regarded as slightly distorted octahedral, which is supported by UV−vis spectroscopy.[61] The other complexes, on the other hand, have an overall symmetry that is weakly distorted tetragonal.[31] From the point of view of fitting the NMRD profile, it turned out that the strategy used for the other complexes did not work satisfactorily for this system. One of the reasons is that the Δ_T and Δ_S values are of similar magnitude; the other reason is symmetry-related and is discussed in detail below.

The initial fits with an axially symmetric transient ZFS gave values of τ_D in the range of 30−43 ps (i.e., a very long time on the time scale of collisions and close to the reorientational correlation time of $\tau_R = 45$ ps). This similarity of the two modulation time scales might be an indication that one motional process would be a sufficient description. Thus, we attempted to fit the NMRD profile with variable R, D_S, and E_S values and kept D_T so small that the distortional modulation would be negligible. This procedure resulted in a rather poor fit in the high-field region (not shown) and yielded values of the ZFS parameters that were inconsistent with the assumed orientation of the ZFS principal axis. To resolve this problem, we decided to abandon the assumption of an axially symmetric transient ZFS. We reported some time ago an interpretation of the NMRD profile for aqueous Ni(II) using a fully rhombic transient ZFS (i.e., $E_T/D_T = 1/3$).[54] We argued for this interpretation on the basis of a combined quantum chemical calculation and molecular dynamics simulation study.[47] By analogy to that study, we tested the assumption that the transient ZFS in Ni([12]aneN$_4$)(H$_2$O)$_2^{2+}$ is fully rhombic, and, in addition, we also performed a fitting for an E_T/D_T ratio of 1/10. It should be stressed that this assumption does not introduce any additional parameters but rather modifies the physical picture. However, we performed four-parameter fittings (R, τ_D, D_T, E_S) rather than three-parameter fittings with different and fixed values of D_T.

The best-fit data of the restricted fittings using different values for E_T/D_T (0, 1/10, 1/3) in the case of the smallest tetraaza complex are collected in Table 7. We found from trial fittings that the value of D_S is close to 1.0 cm^{-1}, and we thus assumed this value in the final fittings. The calculated curves, based on $D_S = 1.0$ cm^{-1} and $\theta = 43°$, are also compared with

TABLE 5: Constrained Three-Parameter (R, τ_D, E_S) Nonlinear Least Squares Fitting at Different Values of D_T for Ni(dpm)$_2$(aniline)$_2^{2+}$ at 32 °C a Using Fixed Value of D_S (5.0 cm^{-1})

	D_T				
	2.0	2.3	2.4	2.5	2.6
R (Å)	3.20 ± 0.02	3.15 ± 0.02	3.14 ± 0.02	3.13 ± 0.03	3.11 ± 0.02
τ_D (ps)	5.4 ± 0.3	5.6 ± 1.4	5.6 ± 1.7	5.8 ± 2.0	5.7 ± 1.4
E_S (cm^{-1})	0.18 ± 0.05	0.09 ± 0.03	0.05 ± 0.03	0.0025 ± 0.0007	0.006 ± 0.008
σ	0.1488	0.1202	0.1161	0.1184	0.1191

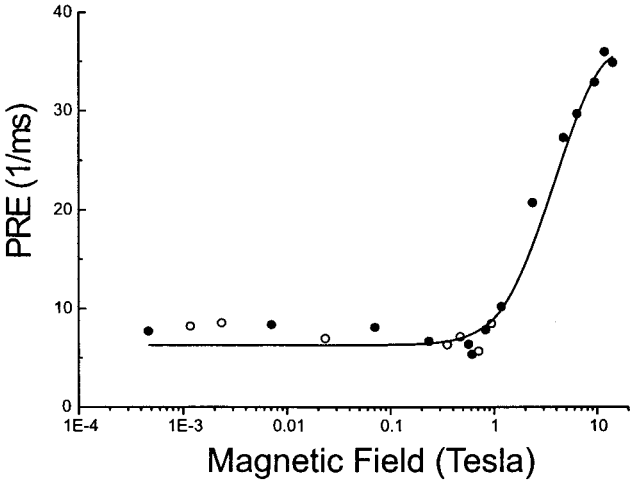

Figure 7. Experimental (symbols) and fitted (line) NMRD profiles for Ni(dpm)$_2$(aniline)$_2^{2+}$ at 32 °C. Experimental points used in the fittings are shown as filled symbols. The fitted curve has been calculated on the basis of the best-fit data in Table 5 for $D_T = 2.4$ cm^{-1}.

experimental data in Figure 9. The quality of the fit for an axially symmetric transient ZFS tensor ($E_T/D_T = 0$) is rather good in terms of the standard deviation of the fit, as we can see from Figure 9. However, as already pointed out, the obtained values for τ_D (37 ps) and D_T (9.7 cm^{-1}) are unreasonably large. At the other extreme, when the ZFS tensor is fully rhombic, we obtained parameter values that seem realistic ($\tau_D = 9.6$ ps and $D_T = 1.6$ cm^{-1}). Here, on the other hand, the quality of the fit is worse than that for the case with an axially symmetric ZFS tensor, particularly in the high-field regime. The case in which the E_T/D_T ratio is 1/10 gives satisfactory parameter values and a relatively good quality of fit (between those of the other two cases). The low-field plateau of the fitted curve for the case of $E_T/D_T = 1/10$ is somewhat better than that for the case corresponding to full rhombicity, but the high-field region is rather similar. One possible explanation of these findings is that our pseudorotation model is not adequate for a fully satisfactory interpretation of this complex. Perhaps a more detailed and explicit description of the contribution from damped vibrational motions to the electron-spin relaxation is needed.

It is interesting, no matter what we assume regarding the symmetry of the transient ZFS tensor, that for this complex the magnitude of Δ_T is larger than that of the static ZFS tensor Δ_S. Thus, it is reasonable to obtain substantial changes in the PRE (or fitted parameter values) when we vary the E_T/D_T ratio, as we observed in the slow-motion calculations in section IV. In agreement with these observations, we obtain a sizable E_S value (0.2 cm^{-1}) for $E_T/D_T = 0$, whereas for a rhombic transient ZFS tensor, the value of E_S becomes negligibly small (see Table 7). Clearly, the complex has very different electron-spin dynamics behavior compared to that of complexes I and II. To our knowledge, this type of feature (i.e., the electron-spin principal frame is more or less determined by the fluctuating transient part of the ZFS rather than by the static part) has not been observed before, which is not surprising because it is an effect that occurs only outside of the Redfield limit.

We also tried to fit the data by setting $\theta = 0°$, but we found no noticeable change in the parameter values, which is due to the small value of the static ZFS parameter D_S. We furthermore checked the effect of varying the angle ϕ by using the best-fit values in Table 7, but we found the change in PRE to be negligible, as expected, because of the insensitivity of the other angle θ.

E. Interpretation of Ni(tmc)(H$_2$O)$^{2+}$ Data. The Ni(tmc)(H$_2$O)$^{2+}$ complex differs from the other systems in that it coordinates only one solvent molecule and is therefore five-coordinated.[25,26] The best-fit data of the restricted fittings using a set of different values for D_T in this complex are collected in Table 8. From trial fittings, we found the value of D_S to be close to 6.0 cm^{-1}, and we thus assumed this value in the final fittings. The calculated curve for $D_T = 6.0$ cm^{-1}, assuming that $D_S = 6.0$ cm^{-1} and $\theta = 13°$ are also compared with the experimental data in Figure 10.

The obtained values of D_T (6.0 cm^{-1}) and τ_D (0.58 ps) are very different from those of the other complexes, which indicates very large flexibility or deformability in this complex. Moreover, it has been reported in the literature[62] that five-coordinated complexes with square-pyramidal ligand fields (C_{4v} symmetry) have energies of states (ground as well as excited states) that are sensitive to relative changes in the in-plane and axial ligand fields. We may therefore expect deviation from that symmetry and hence a rather large rhombicity in the static ZFS. Indeed, we obtain an E_S value of 0.93 cm^{-1}, which is much larger than those for the other complexes. The controlling influence of ZFS rhombicity has been elucidated by Sharp and co-workers.[58] They compared the complexes Ni(en)$_3^{2+}$ and Ni(en)$_2$(H$_2$O)$_2^{2+}$, which have different symmetries of the static ZFS tensor. The ZFS tensor of the former complex is axial, whereas that of the latter is rhombic. They found that, as predicted, the NMRD profile for Ni(en)$_2$(H$_2$O)$_2^{2+}$ has a low-field plateau that is much smaller (about five times) than that for the other complex because of the rhombicity effect. If we make the same comparison between Ni(tmc)(H$_2$O)$^{2+}$ and the other complexes in the present analysis, we find that the low-field PRE for Ni(tmc)(H$_2$O)$^{2+}$ is only about $^1/_4$ of that of the others (taking into account that $q = 1$ in complex IV). This result further supports the rather large value of E_S (0.93 cm^{-1}) for Ni(tmc)(H$_2$O)$^{2+}$ compared to those of the other complexes (0.005−0.05 cm^{-1} for I and II and 0.0003−0.2 cm^{-1} for III, depending on the E_T/D_T ratio).

There is a similarity between this complex and Ni([12]aneN$_4$)(H$_2$O)$_2^{2+}$ regarding the ZFS, namely, that the relative magnitudes of Δ_T and Δ_S are similar in each complex (in fact, $\Delta_T = \Delta_S$ for this complex), even though the individual values for Ni(tmc)(H$_2$O)$^{2+}$ are substantially larger. Thus, the electron-spin dynamics in this complex is similar to that of complex III. We might therefore expect some effects if we vary the E_T/D_T ratio. We explored that possibility, but the parameter values obtained for this complex in the case of a fully rhombic transient ZFS

TABLE 6: Constrained Three-Parameter (R, τ_D, E_S) Nonlinear Least Squares Fitting at Different Values of D_T for Ni([15]aneN$_4$)(H$_2$O)$_2^{2+}$ at 25 °C Using a Fixed Value of D_S (5.0 cm^{-1})

	D_T				
	2.0	2.2	2.3	2.4	2.6
R (Å)	3.13 ± 0.02	3.13 ± 0.02	3.13 ± 0.02	3.13 ± 0.01	3.13 ± 0.02
τ_D (ps)	7.4 ± 1.8	9.2 ± 2.0	10 ± 3	11 ± 2	14 ± 3
E_S (cm^{-1})	0.18 ± 0.02	0.10 ± 0.02	0.05 ± 0.02	0.006 ± 0.001	0.0018 ± 0.0009
σ	0.0534	0.0503	0.0495	0.0505	0.0639

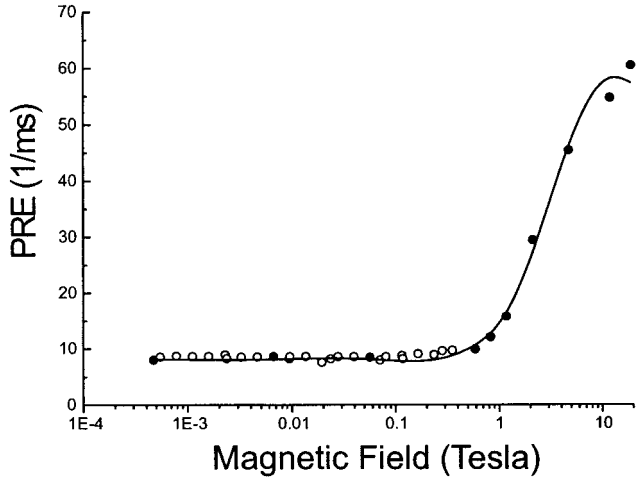

Figure 8. Experimental (symbols) and fitted (line) NMRD profiles for Ni([15]aneN$_4$)(H$_2$O)$_2^{2+}$ at 25 °C. Experimental points used in the fittings are shown as filled symbols. The high-field relaxation rates of the experimental profile have been corrected to account for the dilution with D$_2$O. The fitted curve has been calculated on the basis of the best-fit data in Table 6 for D_T = 2.3 cm^{-1}.

TABLE 7: Constrained Four-Parameter (R, τ_D, D_T, E_S) Nonlinear Least Squares Fitting at Different Values of the E_T/D_T Ratio for Ni([12]aneN$_4$)(H$_2$O)$_2^{2+}$ at 25 °C Using a Fixed Value of D_S (1.0 cm^{-1})

	E_T/D_T		
	0	1/10	1/3
R (Å)	2.91 ± 0.05	3.00 ± 0.03	3.01 ± 0.05
τ_D (ps)	37 ± 8	14 ± 6	9.6 ± 3.6
D_T (cm^{-1})	9.7 ± 2.0	2.5 ± 0.4	1.6 ± 0.2
E_S (cm^{-1})	0.16 ± 0.03	0.02 ± 0.001	0.0003 ± 0.00004
σ	0.0644	0.0770	0.0947

tensor were not very different from those obtained using an axially symmetric transient ZFS. The D_T value decreased to 5.3 cm^{-1}, but the value of Δ_T remained virtually constant (5.0 cm^{-1} for a fully rhombic transient ZFS tensor compared to 4.9 cm^{-1} for the axial case). The values of R and τ_D decreased somewhat (from 3.09 Å and 0.58 ps to 3.01 Å and 0.50 ps, respectively), whereas the value of E_S increased slightly (from 0.93 to 1.07 cm^{-1}) by the inclusion of rhombicity in the transient ZFS. The fitted curve with E_T/D_T = 1/3 (not shown) actually coincides with that of E_T/D_T = 0. The reason we do not see any effects when changing the symmetry of the transient ZFS is probably that Δ_T does not dominate Δ_S as it does in complex III. In addition, the value of E_S is much larger for Ni(tmc)(H$_2$O)$^{2+}$, and E_S is probably what basically determines the features at low magnetic field.

Using the best-fit values in Table 8, we varied the values of θ and ϕ, but no significant changes in the PRE were found. We mentioned in section II that we estimated τ_R from carbon-13 measurements of the similarly sized complex Ni([15]aneN$_4$)(H$_2$O)$_2^{2+}$. To test the sensitivity of this parameter, we performed a fit with a higher value of τ_R (90 ps) for D_S and D_T,

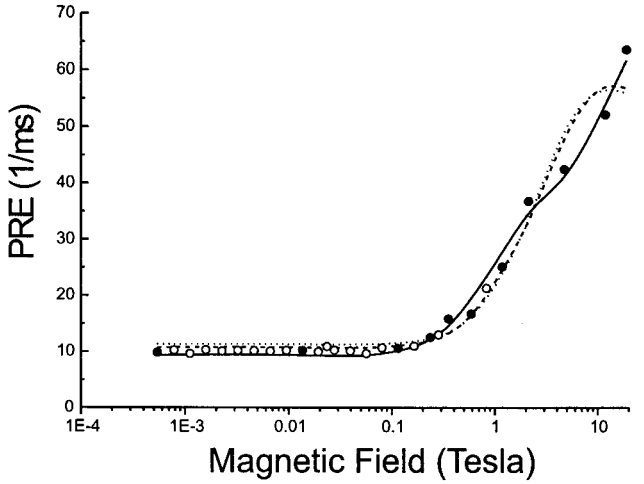

Figure 9. Experimental (symbols) and fitted (lines) NMRD profiles for Ni([12]aneN$_4$)(H$_2$O)$_2^{2+}$ at 25 °C. Experimental points used in the fittings are shown as filled symbols. The high-field relaxation rates of the experimental profile have been corrected to account for the dilution with D$_2$O. The fitted curves have been calculated on the basis of the best-fit data in Table 7 for E_T/D_T ratios of 0 (—), 1/10 (---), and 1/3 (•••).

which are both equal to 6.0 cm^{-1}. We found only small changes in the fitted parameters: R remained the same (3.09 Å), E_S was just outside the error limit (0.91 cm^{-1}), and τ_D decreased from 0.58 to 0.52 ps. In addition, the fitted curves virtually coincide (not shown), and we conclude that the physical picture of a complex with fairly large static ZFS rhombicity and significant deformability is probably correct.

VI. Conclusions

The most recent version of the slow-motion theory includes rhombicity in both the transient and the static part of the ZFS. We illustrate some interesting features in the NMRD profiles of this combined rhombicity effect, which is relevant to the experimental analysis in this article. The main part of the article describes an application of this version of the slow-motion theory (allowing for noncoinciding dipole−dipole and ZFS principal axes and not requiring axial symmetry of the ZFS tensor) to an interpretation of experimental NMRD data for four Ni(II) (S = 1) complexes. The number of experimental points is large, but the number of characteristic features in the data set is limited to the low-field PRE, the frequency at which the PRE starts increasing, the steepness of the increase, and the high-field relaxation rates. Unfortunately, despite measurements up to the highest magnetic fields available on commercial NMR instrumentation (18.8 T), we were not able to reach the expected turning point where the PRE would begin decreasing again with increasing magnetic field.

These limitations in the experimental data sets made it necessary to use restricted fits. Clearly, the strategy described above is not unique. Keeping the value of D_S constant in the final fittings is not very critical to the fits, at least not for

TABLE 8: Constrained Three-Parameter (R, τ_D, E_S) Nonlinear Least Squares Fitting at Different Values of D_T for Ni(tmc)$(H_2O)^{2+}$ at 25 °C Using a Fixed Value of D_S (6.0 cm^{-1})

	D_T				
	5.8	5.9	6.0	6.1	6.2
R (Å)	3.12 ± 0.005	3.10 ± 0.003	3.09 ± 0.002	3.08 ± 0.003	3.06 ± 0.002
τ_D (ps)	0.59 ± 0.01	0.58 ± 0.007	0.58 ± 0.004	0.59 ± 0.007	0.58 ± 0.003
E_S (cm^{-1})	0.87 ± 0.02	0.90 ± 0.01	0.93 ± 0.01	0.95 ± 0.007	0.98 ± 0.007
σ	0.0118	0.0108	0.0096	0.0122	0.0109

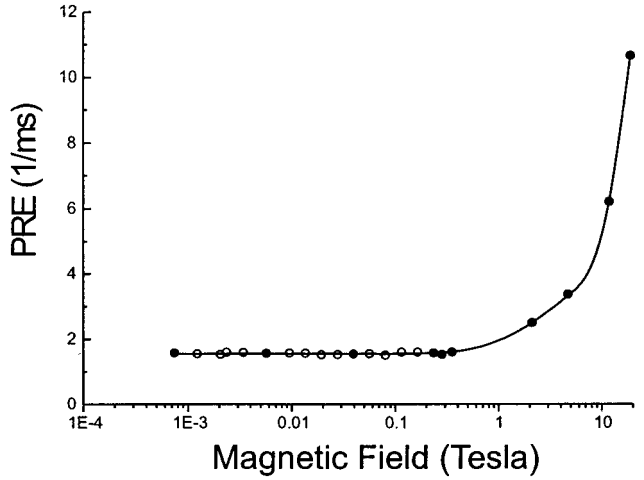

Figure 10. Experimental (symbols) and fitted (line) NMRD profiles for Ni(tmc)$(H_2O)^{2+}$ at 25 °C. Experimental points used in the fittings are shown as filled symbols. The high-field relaxation rates of the experimental profile have been corrected to account for the dilution with D_2O. The fitted curve has been calculated on the basis of the best-fit data in Table 8 for $D_T = 6.0$ cm^{-1}.

complexes I and II. It should be mentioned that these large D_S values are supported by the work of Sharp and co-workers[57,16] and by ab initio calculations.[63] We have validated the correctness of the strategy by a comparison of results obtained at different temperatures for complex I.

The data presented show that the slow-motion theory can be useful as a tool for analyzing experimental NMRD data of paramagnetic transition-metal complexes. The fitted parameters obtained for Ni$(dpm)_2$(aniline-$d_5)_2^{2+}$ and Ni([15]aneN$_4$)-$(H_2O)_2^{2+}$ are surprisingly similar to each other; in fact, the most significant difference is the proton−nickel distance. The second tetraaza complex, Ni([12]aneN$_4$)$(H_2O)_2^{2+}$, has a different ligand-field symmetry, and its NMRD profile indeed requires a different set of parameters. The third tetraaza complex, Ni(tmc)-$(H_2O)^{2+}$, is five-coordinated, resulting in a rather large rhombicity in the static ZFS. The latter two tetraaza complexes exhibit an unusual feature regarding the electron-spin dynamics. The magnitude of the fluctuating transient ZFS is of the same magnitude as the static part of the ZFS, which means that the energy-level structure is at least partially determined by the transient rather than the static ZFS. This result has important consequences for the rhombicity effect and its impact on the PRE. The obtained values of E_S for the different complexes are, in our view, reasonable and seem to reflect the configurations of the complexes and hence the symmetry at the paramagnetic site, which implies that the shape of the NMRD profile is sensitive to the E_S parameter, as has also been observed by Sharp and co-workers in several investigations.[16,57,58] In all four cases, the best-fit parameters are clearly outside the Redfield limit, which means that simpler theories are of limited use.

Acknowledgment. We are indebted to Professor Claudio Luchinat and Professor Ivano Bertini for valuable discussions and comments on the manuscript. We thank Dr. Federica Castellani for assistance with the relaxometers, Dr. Kirill Nerinovski for help with the 90 MHz spectrometer, and Dr. Andrei Kaikkonen for help with the carbon-13 measurements. We are grateful to the Florence Large Scale Facility (LSF) for allowing us to use the field-cycling relaxometers and the high-field NMR spectrometers. This work was supported by the Swedish Natural Science Research Council. Generous grants of computer time by the Center for Parallel Computers in Stockholm are gratefully acknowledged.

References and Notes

(1) Kowalewski, J. In *Encyclopedia of Nuclear Magnetic Resonance*; Grant, D. M., Harris, R. K., Eds.; Wiley & Sons: Chichester, 1996; Vol. 5, pp 3455−3462.
(2) Banci, L.; Bertini, I.; Luchinat, C. *Nuclear and Electron Relaxation*; VCH: Weinheim, 1991.
(3) Bertini, I.; Luchinat, C.; Parigi, G. *Solution NMR of Paramagnetic Molecules*; Elsevier: Amsterdam, 2001.
(4) Swift, T. J.; Connick, R. E. *J. Chem. Phys.* **1962**, *37*, 307.
(5) Bloembergen, N.; Morgan, L. O. *J. Chem. Phys.* **1961**, *34*, 842.
(6) Muller, R. N. In *Encyclopedia of Nuclear Magnetic Resonance*; Grant, D. M., Harris, R. K., Eds.; Wiley & Sons: Chichester, 1996; Vol. 3, pp 1438−1444.
(7) Abragam, A.; Bleaney, B. *Electron Paramagnetic Resonance of Transition Ions*; Clarendon Press: Oxford, 1970.
(8) Lindner, U. *Ann. Phys. (Leipzig)* **1965**, *16*, 319.
(9) Bertini, I.; Luchinat, C.; Mancini, M.; Spina, G. *J. Magn. Reson.* **1984**, *59*, 213.
(10) Banci, L.; Bertini, I.; Briganti, F.; Luchinat, C. *J. Magn. Reson.* **1986**, *66*, 58.
(11) Bertini, I.; Galas, O.; Luchinat, C.; Parigi, G. *J. Magn. Reson.* **1995**, *113*, 151.
(12) Sharp, R.; Lohr, L.; Miller, J. *Prog. Nucl. Magn. Reson. Spectrosc.* **2001**, *38*, 115.
(13) Sharp, R. R. *J. Chem. Phys.* **1993**, *98*, 6092.
(14) Bovet, J.-M.; Sharp, R. R. *J. Chem. Phys.* **1993**, *99*, 18.
(15) Abernathy, S. M.; Miller, J. C.; Lohr, L. L.; Sharp, R. R. *J. Chem. Phys.* **1998**, *109*, 4035.
(16) Sharp, R.; Abernathy, S. M.; Lohr, L. L. *J. Chem. Phys.* **1997**, *107*, 7620.
(17) Bertini, I.; Kowalewski, J.; Luchinat, C.; Nilsson, T.; Parigi, G. *J. Chem. Phys.* **1999**, *111*, 5795.
(18) Abernathy, S. M.; Sharp, R. R. *J. Chem. Phys.* **1997**, *106*, 9032.
(19) Westlund, P.-O. In *Dynamics of Solutions and Fluid Mixtures by NMR*; Delpuech, J. J., Ed.; Wiley & Sons: Chichester, 1995; Chapter 4, pp 173−229.
(20) Nilsson, T.; Svoboda, J.; Westlund, P.-O.; Kowalewski, J. *J. Chem. Phys.* **1998**, *109*, 6364.
(21) Nilsson, T.; Kowalewski, J. *J. Magn. Reson.* **2000**, *146*, 345.
(22) Larsson, T.; Westlund, P.-O.; Kowalewski, J.; Koenig, S. H. *J. Chem. Phys.* **1994**, *101*, 1116.
(23) Busch, D. H. *Acc. Chem. Res.* **1978**, *11*, 392.
(24) Scott, B.; Brewer, K. J.; Spreer, L. O.; Craig, C. A.; Otvos, J. W.; Calvin, M.; Taylor, S. *J. Coord. Chem.* **1990**, *21*, 307.
(25) Barefield, E. K.; Wagner, F. *Inorg. Chem.* **1973**, *12*, 2435.
(26) Iwamoto, E.; Nishimoto, J.; Yokoyama, T.; Yamamoto, K.-I.; Kumamaru, T. *J. Chem. Soc., Faraday Trans.* **1991**, *87*, 1537.
(27) Moore, P.; Sachinidis, J.; Willey, G. R. *J. Chem. Soc., Chem. Commun.* **1983**, 522−523.
(28) Crick, I. S.; Tregloan, P. A. *Inorg. Chim. Acta* **1988**, *142*, 291.
(29) Coates, J. H.; Hadi, D. A.; Lincoln, S. F.; Dodgen, H. W.; Hunt, J. P. *Inorg. Chem.* **1981**, *20*, 707.
(30) Hung, Y.; Martin, L. Y.; Jackels, S. C.; Tait, A. M.; Busch, D. H. *J. Am. Chem. Soc.* **1977**, *99*, 4029.
(31) Martin, L. Y.; Sperati, R. C.; Busch, D. H. *J. Am. Chem. Soc.* **1977**, *99*, 2968.
(32) Otting, G. *J. Magn. Reson.* **1994**, *103*, 288.

(33) Kowalewski, J.; Nordenskiöld, L.; Benetis, N.; Westlund, P.-O. *Prog. Nucl. Magn. Reson. Spectrosc.* **1985**, *17*, 141.
(34) Benetis, N.; Kowalewski, J.; Nordenskiöld, L.; Wennerström, H.; Westlund, P.-O. *Mol. Phys.* **1983**, *48*, 329.
(35) Wangsness, R. K.; Bloch, F. *Phys. Rev.* **1953**, *89*, 728.
(36) Bloch, F. *Phys. Rev.* **1956**, *102*, 104.
(37) Redfield, A. G. *IBM J. Res. Dev.* **1957**, *1*, 19.
(38) Redfield, A. G. *Adv. Magn. Reson.* **1965**, *1*, 1.
(39) Slichter, C. P. *Principles of Magnetic Resonance*, 3rd ed.; Springer-Verlag: Berlin, 1992.
(40) Brink, D. M.; Satchler, G. R. *Angular Momentum*, 2nd ed.; Clarendon Press: Oxford, 1979.
(41) *Electron Spin Relaxation in Liquids*; Muus, L. T., Atkins, P. W., Eds. Plenum Press: New York, 1972.
(42) Jeener, J. *Adv. Magn. Reson.* **1982**, *10*, 1.
(43) Blum, K. *Density Matrix Theory and Applications*; Plenum Press: New York, 1989.
(44) Lanczos, C. *J. Res. Natl. Bur. Stand. (U.S.)* **1952**, *49*, 33.
(45) Chandler, J. *Behav. Sci.* **1969**, *14*, 81.
(46) De Tar, D. F. In *Computer Programs for Chemistry*; Wiberg, K. B., Ed.; Academic Press: New York, 1972; Vol. 4, Chapter 3, pp 71−123.
(47) Odelius, M.; Ribbing, C.; Kowalewski, J. *J. Chem. Phys.* **1995**, *103*, 1800.
(48) Wertz, J. E.; Bolton, J. R. *Electron Spin Resonance: Elementary Theory and Practical Applications*; McGraw-Hill: New York, 1972.
(49) Fukui, H.; Miura, K.; Matsuda, H. *J. Magn. Reson.* **1990**, *88*, 311.
(50) Dwek, R. A. *Nuclear Magnetic Resonance in Biochemistry*; Clarendon Press: Oxford, 1975.
(51) Burton, D. R.; Forsén, S.; Karlström, G.; Dwek, R. A. *Prog. Nucl. Magn. Reson. Spectrosc.* **1979**, *13*, 1.
(52) Kowalewski, J.; Laaksonen, A.; Nordenskiöld, L.; Saunders, V. R. *J. Magn. Reson.* **1983**, *53*, 346.
(53) Carrington, A.; Luckhurst, G. R. *Mol. Phys.* **1964**, *8*, 125.
(54) Svoboda, J.; Nilsson, T.; Kowalewski, J.; Westlund, P.-O.; Larsson, P. T. *J. Magn. Reson.* **1996**, *121*, 108.
(55) Nilsson, T. Ph.D. Thesis, Stockholm University, Edsbruk, Sweden, 2000.
(56) Westlund, P.-O.; Larsson, T. P.; Teleman, O. *Mol. Phys.* **1993**, *78*, 1365.
(57) Abernathy, S. M.; Sharp, R. R. *J. Phys. Chem.* **1997**, *101*, 3692.
(58) Miller, J. C.; Lohr, L. L.; Sharp, R. R. *J. Magn. Reson.* **2001**, *148*, 267.
(59) Nilsson, T.; Kowalewski, J. *Mol. Phys.* **2000**, *98*, 1617. Erratum: Nilsson, T.; Kowalewski, J. *Mol. Phys.* **2001**, *99*, 369.
(60) Friedman, H. L.; Holz, M.; Hertz, H. G. *J. Chem. Phys.* **1979**, *70*, 3369.
(61) Craig, C. A.; Spreer, L. O.; Otvos, J. W.; Calvin, M. *J. Phys. Chem.* **1990**, *94*, 7957.
(62) Ciampolini, M. *Inorg. Chem.* **1966**, *5*, 35.
(63) Ribbing, C.; Odelius, M.; Kowalewski, J.; Pettersson, L. *Theor. Chim. Acta* **1994**, *87*, 307.